This is a repository copy of *Analysis of consequent-pole flux reversal permanent magnet machine with biased flux modulation theory*.

White Rose Research Online URL for this paper:
https://eprints.whiterose.ac.uk/146757/

Version: Accepted Version

Article:

Yang, H., Zhu, Z.Q. orcid.org/0000-0001-7175-3307, Lin, H. et al. (2 more authors) (2020) Analysis of consequent-pole flux reversal permanent magnet machine with biased flux modulation theory. IEEE Transactions on Industrial Electronics, 67 (3). pp. 2107-2121. ISSN 0278-0046

https://doi.org/10.1109/tie.2019.2902816

© 2019 IEEE. Personal use of this material is permitted. Permission from IEEE must be obtained for all other users, including reprinting/ republishing this material for advertising or promotional purposes, creating new collective works for resale or redistribution to servers or lists, or reuse of any copyrighted components of this work in other works. Reproduced in accordance with the publisher's self-archiving policy.

Reuse

Items deposited in White Rose Research Online are protected by copyright, with all rights reserved unless indicated otherwise. They may be downloaded and/or printed for private study, or other acts as permitted by national copyright laws. The publisher or other rights holders may allow further reproduction and re-use of the full text version. This is indicated by the licence information on the White Rose Research Online record for the item.

Takedown

If you consider content in White Rose Research Online to be in breach of UK law, please notify us by emailing eprints@whiterose.ac.uk including the URL of the record and the reason for the withdrawal request.

eprints@whiterose.ac.uk
https://eprints.whiterose.ac.uk/

Analysis of Consequent-Pole Flux Reversal Permanent Magnet Machine with Biased Flux Modulation Theory

***Abstract*—This paper investigates a consequent-pole flux reversal machine (CP-FRM) with biased flux modulation theory, which employs homopolar permanent magnets (PMs) placed between the adjacent stator poles. The machine topology is introduced from the perspective of FRM with a shifted magnet position and CP arrangement, and the performance comparison between the proposed CP-FRM and its original surface-mounted PM (SPM) counterpart is presented to highlight the torque improvement of the CP structure. Then, a simplified permeance model is applied to the CP-FRM to identify the principal effective air-gap field harmonics engaging in the torque productions. It shows that the CP-FPM works based on a biased flux modulation effect due to its asymmetric air-gap field distribution caused by the CP configuration, which unveils its underlying torque improvement mechanism over its SPM-FRM counterpart. In order to obtain the highest torque capability, the key design parameters are analytically optimized by analyzing the winding configuration, which aids the establishment of a general design guideline for the CP-FRM. The analytical and FE results are validated by the experiments.**

***Index Terms*—Consequent pole, doubly salient, flux reversal machine, magnetic gearing effect, permanent magnet (PM), switched reluctance.**

I. INTRODUCTION

DUE TO the absence of permanent magnets (PMs) and windings on rotor, switched reluctance machines (SRMs) [1] have been widely used in domestic appliances and more-electrical aircraft, etc. The merits of low cost, fault tolerance, simple rotor make SRMs suitable for critical-safety applications. Nevertheless, due to the influence of unipolar non-sinusoidal excitation, non-conventional drive circuit and doubly salient structure, SRMs suffer from high torque ripple, acoustic noise and vibration [2].

In order to overcome the above drawbacks, several PM-assisted methods are recently employed in SRMs [3]-[17] [20]-[24]. As a typical and simple PM-assisted solution, flux reversal machines (FRMs) [7]-[17] [20]-[24] have been of increasing research interest in the last decade, of which PMs are placed on their stator pole surface. Apart from inheriting simple salient rotor structure of SRMs [1], the merits of easy thermal management, alleviated torque ripple issue, as well as increased torque density can be obtained with FRMs. More importantly, since the variable reluctance behavior induces bipolar and sinusoidally varied flux linkage, FRMs can behave in a similar way as brushless AC synchronous PM machines. Consequently, the well-developed AC vector control methods can be employed rather than the asymmetric bridge converter typical for SRMs. Taking the two FRMs with 6 stator slots as an instance, as illustrated in Fig. 1, ether one can be geometrically considered as a SRM plus an additional biased PM ring. In this case, we can define a PM-biased angle θ_{mw} as the angle between the central axes of PM poles relative to coil A_1. Hence, the FRM with "θ_{mw}=15°" refers to well-known conventional structure (named as SPM-FRM-I) [7]-[17]. On the other hand, if θ_{mw}=0° or 30°, a new FRM with shifted relative PM position can be obtained, which is termed as SPM-FRM-II.

The flux leakage issue is a major concern in the above FRMs, which restricts the torque density. Meanwhile, rare-earth PM material, such as NdFeB, is very expensive, and suffers from limited resources so that the consequent-pole (CP) PM design concept [18] [19] is recently extended to FRMs [20]-[24] by replacing nearly half PMs with iron poles. In addition, PM irreversible demagnetization risk is reduced due to the existence of iron poles on the stator surface. Based on the aforementioned FRMs with different PM-biased angles ranging from 0° to 30°, several available CP-FRMs can be correspondingly developed [20]-[24], as illustrated in Fig. 2.

Based on the SPM-FRM-I [7]-[17], a corresponding CP configuration is presented in [20] [21], as shown in Fig. 2(a). In [21], the influence of different CP arrangements on the electromagnetic performance of CP-FRMs is investigated, which suggests the torque capability can be further enhanced by selecting an appropriate CP structure. Besides, when multiplying the PM segments per stator pole, several alternative CP-FRMs are developed so as to further improve the torque density [22]. Overall, it shows that the CP-FRMs exhibit higher torque, whereas their magnet usages are only half of those of the regular FRMs [20].

On the other hand, as PMs are placed on the centers of stator poles, another CP-FRM can be obtained from the SPM-FRM-II (θ_{mw}=0°), as shown in Fig. 2(b), termed as CP-FRM-II. Alternately, the CP-FRM (see Fig. 2(c)) investigated in this paper is developed from the SPM-FRM-II with "θ_{mw}=30°", termed as CP-FRM-III. Different from the existing structures [20]-[24], the ferromagnetic iron poles of the proposed CP-FRM are located on the middle positions of stator poles (θ_{mw}=30°), which makes the stator and rotor laminations similar to those of SRMs.

The main contribution of this paper lies in the investigation of the consequent pole flux reversal PM machine with a new biased flux modulation theory. The novelty of this paper can be summarized as follows: 1) a novel analytical modeling method for consequent pole flux reversal PM machines is employed to identify and quantify the primitive air-gap field harmonics contributing to the torque generation. It can be found that the asymmetric air-gap field distribution results in more abundant harmonics induced from the even-order PM fields, which can be termed as "biased flux modulation theory" that is absent in the existing literatures [23]-[25]; 2) the underlying reason of the torque performance improvement of the consequent pole topology over the conventional SPM counterparts is revealed; 3) the detailed design principle for the CP FRMs is presented based on the analytical modeling.

Although the particular variable flux cases of the consequent pole FRM are reported in [23]-[25], an in-depth understanding of the torque production mechanism as well as detailed design principle for the NdFeB PM based CP-FRMs are still unexplored hitherto.

This paper will be organized as follows: in Section II, a typical CP-FRM topology is described, and the performance comparison between the CP-FRM and its original SPM-FRM-II counterpart is presented. Then, in Section III, a simplified analytical model is established to reveal the underlying torque production mechanism of the CP-FRM. Section IV is devoted to the investigation on design principle of the CP-FRM by using the analytical model. Finally, some test measurements are presented to validate the FE and analytical results in Section V.

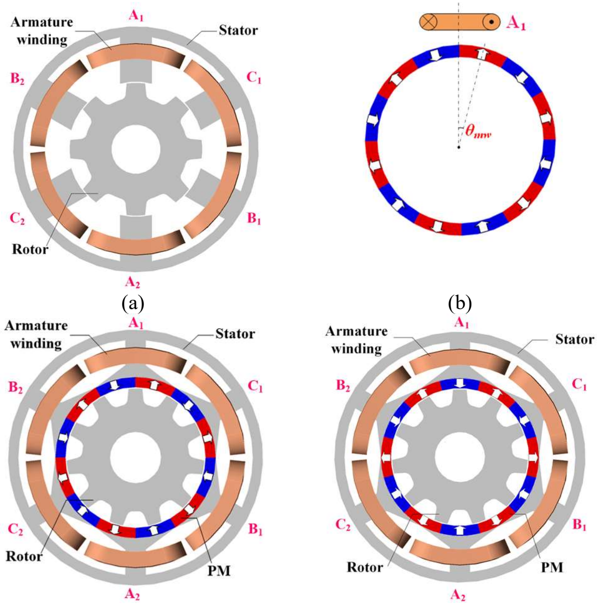

(a) (b) (c) (d)

Fig. 1. Topologies of SPM-FRMs derived from SRM. (a) SRM. (b) PM ring. (c) SPM-FRM-I, θ_{mw}=15° (conventional). (d) SPM-FRM-II, θ_{mw}=30° (new).

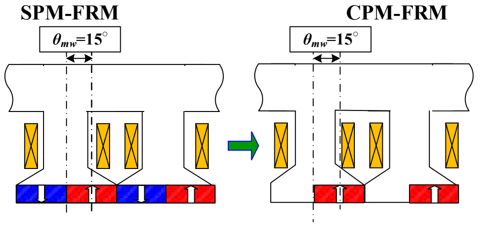

(a)

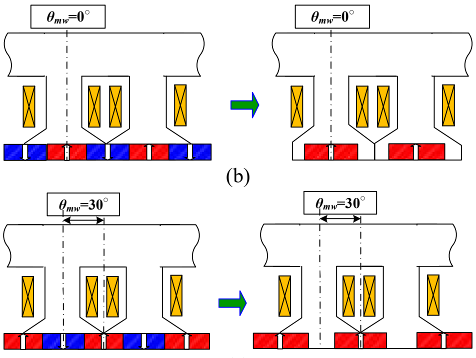

(b)

(c)

Fig. 2. Illustration of various CP-FRMs based on (a) SPM-FRM-I, θ_{mw}=15° (CP-FRM-I). (b) SPM-FRM-II, θ_{mw}=0°. (CP-FRM-II) (c) SPM-FRM-II, θ_{mw}=30°. (CP-FRM-III)

II. FRMs WITH SPM AND CP CONFIGURATIONS

A. Machine Topology

By way of example, the topology of the typical CP-FRM (model-III) is shown in Fig. 3 by replacing half of PMs with iron poles based on SPM-FRM-II. The machine can be also geometrically considered as a conventional SRM with the diametrically magnetized PMs between adjacent stator poles. The PMs are with the same magnetization directions, forming a CP configuration. Meanwhile, the existence of ferromagnetic poles makes the diametrically magnetized PMs less exposed to irreversible demagnetization threats. In addition, it can be observed that the stator and rotor laminations of the CP-FRM are similar to those doubly salient structure of SRMs, which permits simplicity, robustness and ease of manufacture.

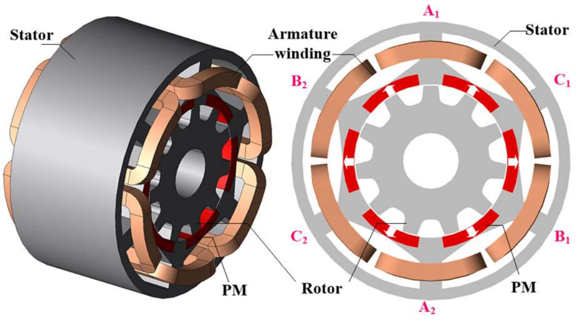

(a) (b)

Fig. 3. Topology of the typical CP-FRM. (a) 3D-view. (b) Cross-section.

TABLE I
DESIGN PARAMETERS OF 6/11-POLE FRMS WITH SPM AND CP ARRANGEMENTS

Machine types	Unit	SPM	CP
Rated speed	r/min	400	
Rated current	Arms	7.5	
Stator outer diameter	mm	100	
Air-gap length	mm	0.5	
Active stack length	mm	50	
Split ratio	-	0.55	
Stator back-iron thickness	mm	4.5	
Stator tooth width	mm	8.5	
Rotor pole height	mm	4.5	
Ratio of rotor pole to pitch	-	0.38	0.33
NdFeB magnet thickness	mm	4	
Magnet pole arc	deg	30	43.2
Magnet usage	mm^3	34557.5	24881.4
Magnet grade	-	N35SH	

B. Comparative Study

The 6/11-pole CP-FRM is taken as an example for the following performance comparison with its SPM counterpart. The major design parameters of the two machines are listed in Table I. It should be noted that the two investigated machines share identical overall dimensions and current condition, etc. for a fair comparison.

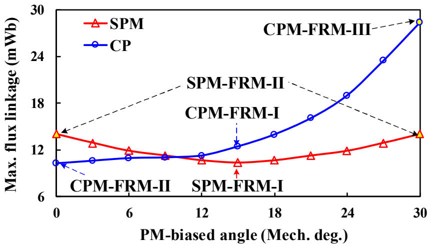

Fig. 4. Relation between axis angle and maximum phase flux linkages of the 6/11-pole SPM- and CP-FRMs.

1) Open-Circuit Performance

In order to highlight the advantages of the developed CP-FRM, as well as obtain the optimal PM-biased angle, the phase flux linkages of the SPM- and CP-FRMs as functions of θ_{mw} are shown in Fig. 4. It can be seen that the optimal θ_{mw} for maximizing the flux linkage is 30 mechanical degrees for both SPM- and CP-FRMs due to less flux leakage, as evidenced in the open-circuit flux lines shown in Fig. 5. Thus, the SPM- and CP-FRMs with optimal shifted θ_{mw} of 30° are chosen as the focuses of this paper.

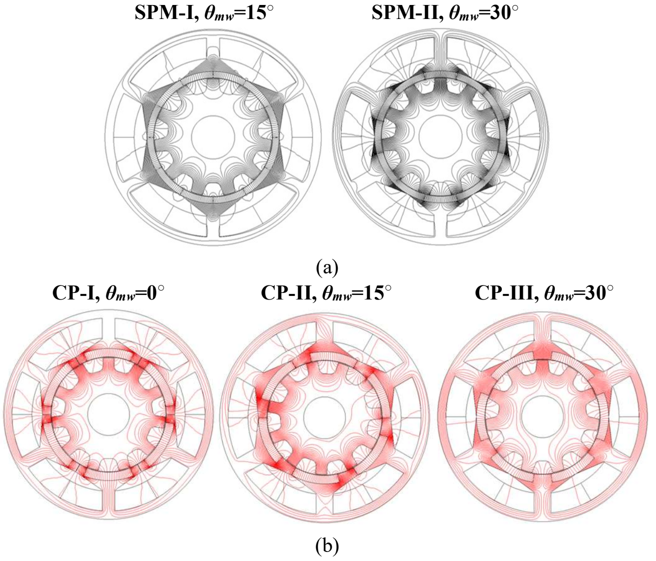

(a)

(b)

Fig. 5. Open-circuit field distributions of (a) SPM- and (b) CP-FRMs with different PM-biased angles.

2) Torque Performance

The on-load torque characteristics of all the FRM models having SPM and CP structures are shown in Fig. 6. It implies that zero d-axis current control is appropriate to maximize the torque regardless of the PM structures. In addition, the average torque and torque ripple results of all the SPM- and CP-FRMs shown in Fig. 5 are tabulated in Table II. It demonstrates that with the identical current, the CP-FRM-III can deliver the highest average torque with the lowest torque ripple by using even 28% lower magnet usage than the SPM-FRM-II. Meanwhile, the SPM-FRM-II shows slightly higher torque capability than the SPM-FRM-I. The highest torque ripple can be observed in the CP-I and CP-II models. This is mainly due to the fact that the CP-FRM-III shows significantly lower flux leakage than its SPM counterpart, as illustrated in Fig. 5. As a result, the CP-FRM-III is selected for further investigation, which is termed as CP-FRM for simplicity in the following Sections. The underlying torque improvement mechanism of the CP-FRM will be revealed and detailed later.

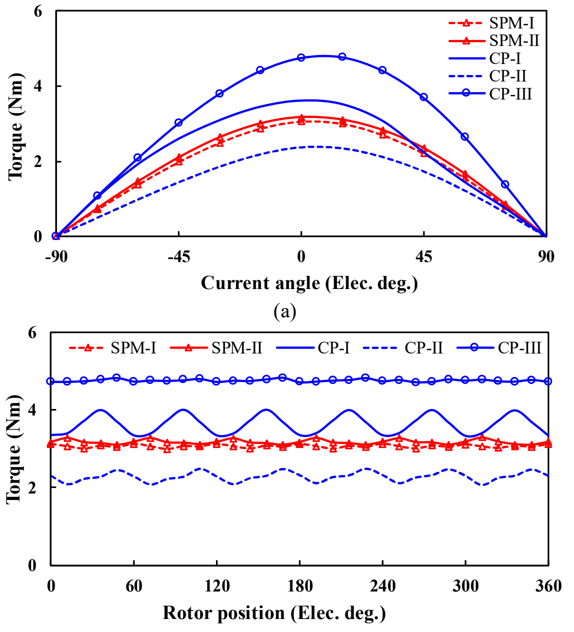

(a)

(b)

Fig. 6. Torque characteristics of the 6/11-pole SPM- and CP-FRMs. (a) Torque versus current angle. (b) Steady-state torque.

TABLE II
COMPARISON OF TORQUE CHARACTERISTICS OF 6-STATOR-SLOT SPM AND CP-FRMS UNDER RATED-LOAD OPERATION

Model	Average torque (N·m)	Torque ripple (%)
SPM-I	3.06	4.53
SPM-II	3.18	6.17
CP-I	3.62	18.92
CP-II	2.28	18.09
CP-III	**4.76**	**2.44**

3) Thermal Analyses

Since the NdFeB PMs are close to the stator poles and windings, which are usually the hot spots, the thermal behaviors of the two FRMs should be accordingly evaluated. A 3-D FE thermal model is developed to perform the thermal analyses of the two machine models. For reducing the computation resource requirement, some assumptions or simplifications are made. First, both the FRMs naturally air-cooled; the end windings are modelled as a torus entity; the heat transferred to all the air regions is uniformly distributed, and hence, all the thermal transfer branches join together at the air regions [26].

The temperature distributions of the SPM- and CP-FRMs under rated-load operation are shown in Fig. 7. The ambient temperature is assumed to be 20 °C. For the SPM case, the peak temperate can be observed in the armature windings, which is approximately 101.2 °C. Meanwhile, the hottest spot of the PM can be found in the right side, ~71.1 °C. The relatively poor airflow and better convection heat transfer conditions of the left-side enclosure are mainly responsible for this. On the other hand, the highest temperatures of the CP counterparts are 97.0 °C and 38.6 °C, respectively. The overall temperature of the CP-FRM is higher than that of the SPM-FRM, which is mainly attributed to the larger winding volume and higher heat flow density of the CP case.

4) PM Demagnetization Withstand Capability

In order to examine the PM demagnetization withstanding capability of the CP-FRM, the operating point distributions and variations of five typical PM points under rated load and 80ºC are shown in Fig. 8. It shows that all the PM working points exceeds the irreversible demagnetization threshold value. That is to say, the on-load accidental PM demagnetization can be well prevented. In fact, it should be mentioned that one advantage of the stator PM machine over the conventional rotor PM machine the easy thermal management and heat dissipation if a better cooling technique is employed in the practical applications [26].

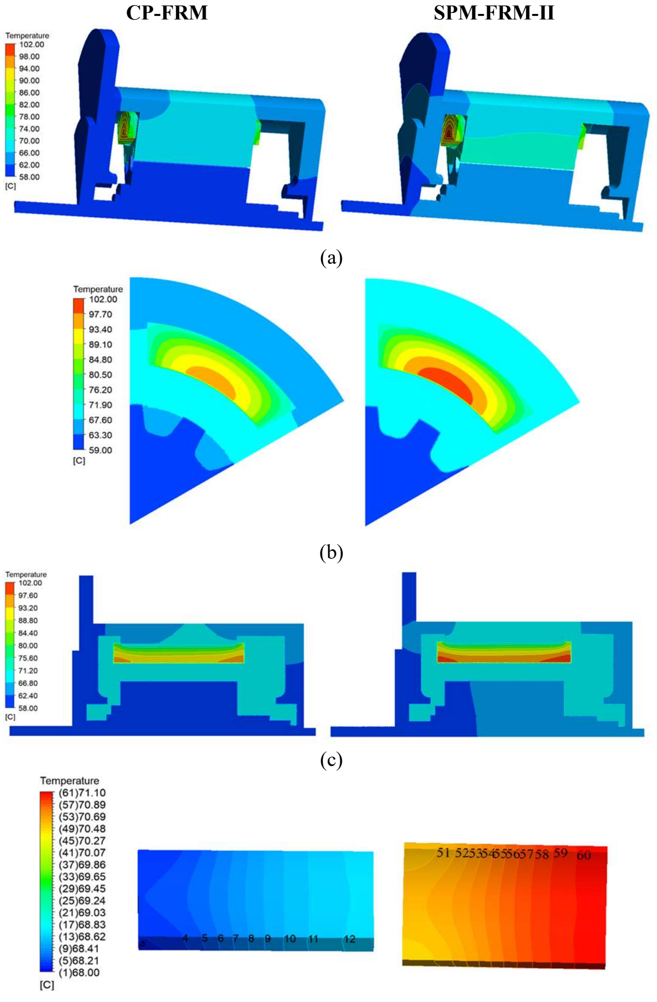

(a)

(b)

(c)

(d)

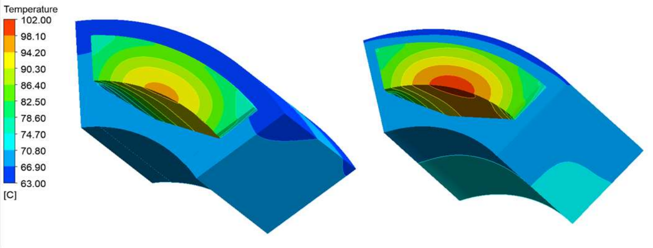

(e)

Fig. 7. The temperature contours @ 400r/min and rated load. (a) The overall view. (b) The radial cutaway view. (c) The tangential cutaway view. (d) The PM temperature fields. (e) The armature winding.

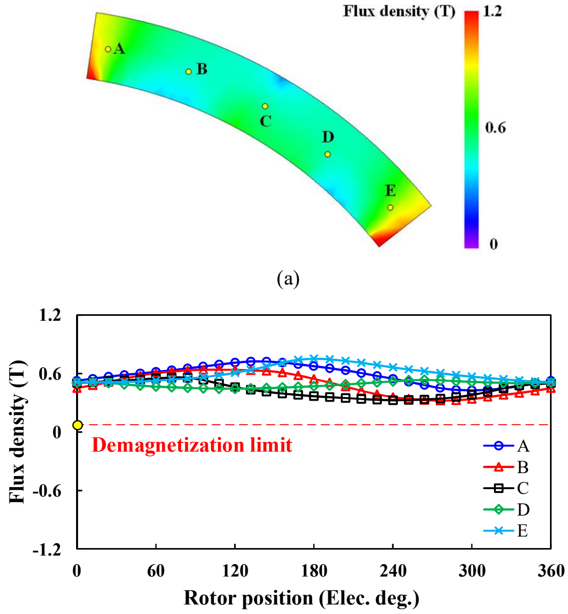

(a)

(b)

Fig. 8. Examination of PM demagnetization withstand capability @ Rated-load, 80ºC. (a) PM field distributions. (b) PM working point variation.

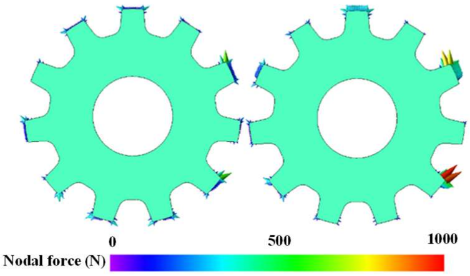

(a) (b)

Fig. 9. The rotor nodal force distributions @ 400r/min and rated load. (a) SPM-FRM-II. (b) CP-FRM.

5) Mechanical Aspects

The rotor mechanical stress characteristics of the FRMs having SPM and CP structures are evaluated. Fig. 9 shows the nodal force results of the two FRMs. It shows that the maximum force values for the two machines are 609.02N and 968.75N, respectively. Subsequently, the radial and tangential stress distributions of the two machines under rated load as well as speed are obtained by inputting the force results into the 3D FE model built in ANSYS Workbench, as shown in Fig. 10. The corresponding stress versus speed waveforms are shown in Fig.

11. It shows that both the stresses increase steadily with the speed rises. Besides, a higher tangential stress can be observed in the CP case, while the SPM-FRM shows higher radial stress.

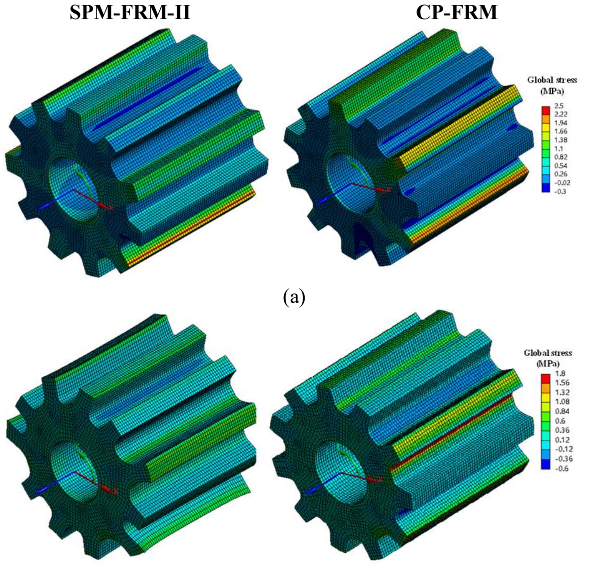

(a)

(b)

Fig. 10. The rotor mechanical stress distributions @ 400r/min and rated load. (a) Radial stress. (b) Tangential stress.

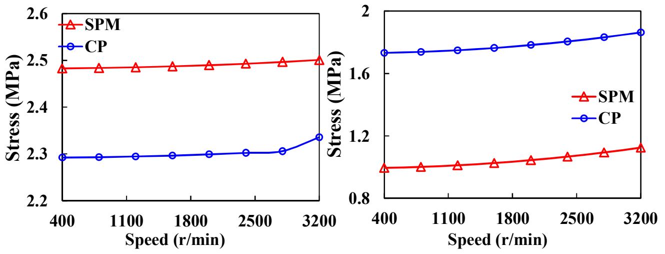

(a) (b)

Fig. 11. The mechanical stress against speed waveforms under rated load. (a) Radial stress. (b) Tangential stress.

III. INVESTIGATION OF WORKING MECHANISM

A. Operating Principle

The operating principle of CP-FRM can be understood from two perspectives. First, the periodical alignment and misalignment between stator and rotor poles result in the bipolar varied flux-linkage, as shown in Fig. 12. It is worth mentioning that the coil flux linkage is non-sinusoidal due to the unbalanced magnetic fluxes from the PM and iron poles. Nevertheless, the resultant phase flux linkage is still sinusoidal and symmetrical by connecting individual coils of the same phase in opposite directions [21], as shown in Fig. 13. That is to say, the cancellation of those even-order harmonics existed in either coil A1 or A2 occurs as evidenced in Fig. 13(b).

Secondly, a CP-FRM can be considered as a flux-modulation machine working based on “magnetic-gearing (MG) effect” [14] [26]-[29]. As illustrated in Fig. 14, the CP-FRM can be divided into three layers, i.e., the stator teeth, the CP modulation poles, and the salient rotor poles. The stationary magnetic fields produced by the PMs are modulated by the rotating iron poles, yielding abundant air-gap field harmonics which are directly engaged in the torque generation.

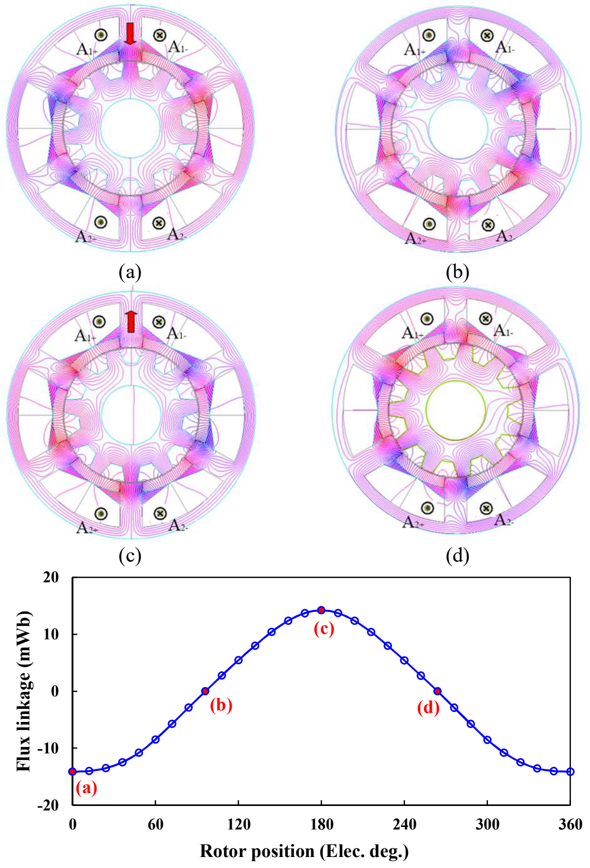

(a) (b)

(c) (d)

(e)

Fig. 12. Operating principle of the 6/11-pole CP-FRM. (a) θ_e=0°. (b) θ_e=90°. (c) θ_e=180°. (d) θ_e=270°. (e) Resultant coil flux linkage waveform.

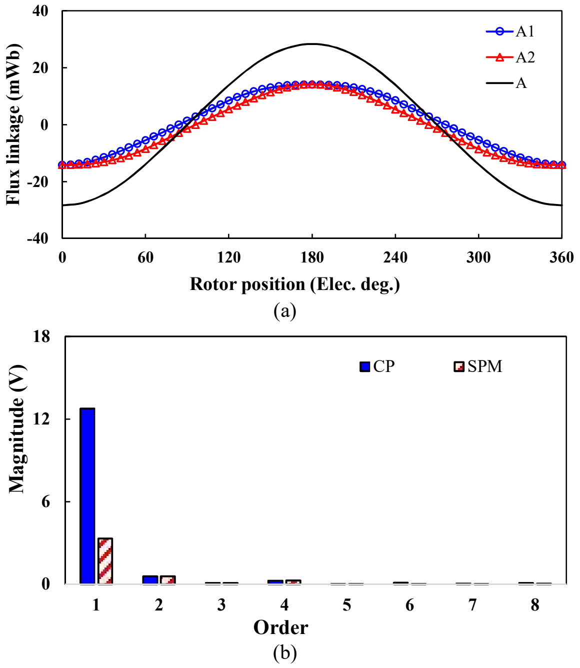

(a)

(b)

Fig. 13. The flux-linkage characteristics of 6/11-pole CPRM. (a) Resultant phase-A flux linkage. (b) Harmonic spectra.

B. Biased Flux Modulation Theory

(1) Analytical Modeling

The ideal air-gap flux density models for the SPM-FRM-II and the developed CP-FRM are plotted in Fig. 15 in order to illustrate the underlying mechanism for the torque improvement with the CP design.

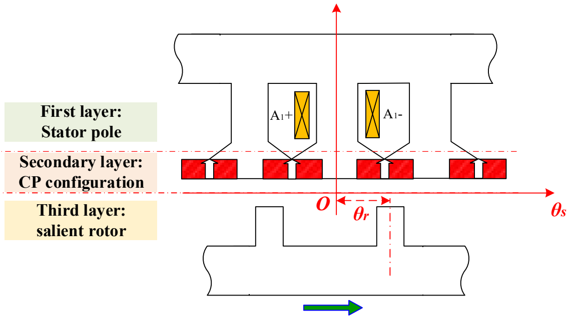

Fig. 14. Illustration of analytical model of the CP-FRM.

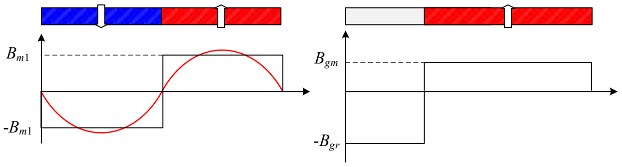

(a) (b)

Fig. 15. Illustration of ideal air-gap flux density distributions of (a) SPM-FRM-II, and (b) CP-FRM.

The ideal air-gap flux density distribution $B_m(\theta_s)$ ignoring the rotor slotting effect can be expressed as its Fourier series expansion [17] [29]

$$B_m(\theta_s)=\sum_i B_i\cos(iN_s\theta_s) \qquad \text{□□□}(1)$$

where N_s is the stator slot number, i is the order of Fourier series, B_i is the corresponding Fourier coefficient, and "θ_s" denotes the angular degree of a particular position in the stator with respect to the phase A winding axis. For the SPM-FRM-II, the magnitude of air-gap flux density B_{m1} can be represented by [19]

$$B_{m1}=\frac{B_r}{1+\mu_r\dfrac{g}{h_m}} \tag{2}$$

where g is the air-gap length, B_r is the remanence flux density of PM, h_m is the PM thickness, and μ_r is the magnet relative permeability. On the other hand, for the developed CP-FRM, the ideal air-gap flux density without accounting for the rotor slotting is defined by B_{m2}, which can be expressed as

$$B_{m2}=\frac{2N_s}{\pi}\left[\begin{array}{l}-\int_0^{\frac{\pi\beta_s}{N_s}}B_{gr}\cos\left(iN_s\theta_s\right)\mathrm{d}\theta_s\\ +\int_{\frac{\pi\beta_s}{N_s}}^{\frac{\pi}{N_s}}B_{gm}\cos\left(iN_s\theta_s\right)\mathrm{d}\theta_s\end{array}\right] \qquad \text{□□□}(3)$$

where B_{gm} and B_{gr} are respectively defined as the air-gap flux density magnitudes of PM and iron poles, i.e.,

$$B_{gm}=\frac{B_r}{1+\mu_r\dfrac{g}{h_m\left(1-\beta_s\right)}} \tag{4}$$

$$B_{gr}=\frac{\beta_s}{1-\beta_s}\times B_{gm}=\frac{\beta_s B_r}{1-\beta_s+\mu_r\dfrac{g}{h_m}} \tag{5}$$

where β_s is the pole-arc ratio, denoting the ratio of the PM arc angle to the stator arc angle per pole. Fig. 16 shows the analytically and FE predicted air-gap flux density waveforms and harmonic spectra without considering slotting effect. It shows that the analytically predicted peak flux densities based on (2)~(5) agree well with the FE results, which confirms the correctness of the above analytical model. Besides, the air-gap flux density distributions of the CP configuration appear to be asymmetric. It indicates that the CP-FRM can produce a series of air-gap harmonics with even-order multiples of PM pole pairs, i.e., kN_s, k=2, 4, 6…, which are absent in the air-gap field harmonics of the conventional SPM structure with uniform N-S magnet poles. That is to say, the CP-FRM is capable of involving more working harmonics in torque production, as will be detailed later.

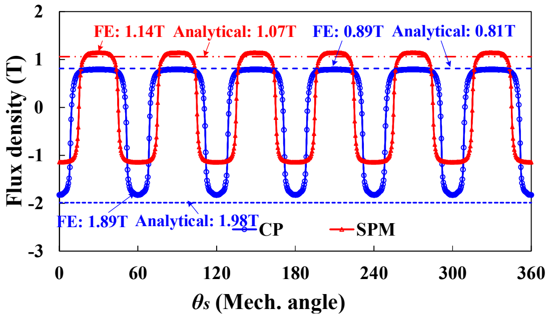

(a)

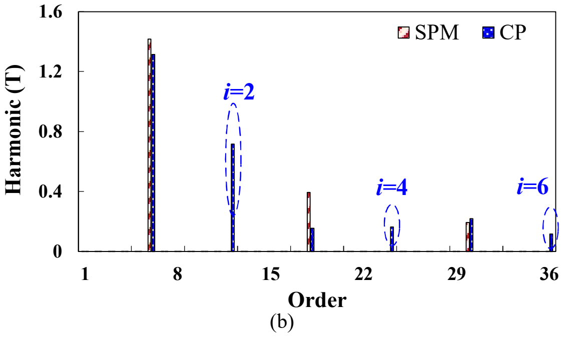

(b)

Fig. 16. Comparison of open-circuit air-gap flux density waveforms without accounting for slotting effect. (a) Waveforms. (b) Harmonic spectra.

In addition, the air-gap permeance $\Lambda_r(\theta_s, \theta_r)$ considering the rotor slotting can be given as

$$\Lambda_r\left(\theta_s,\theta_r\right)=\frac{\mu_0}{g+\delta(\theta_s,\theta_r)}=\Lambda_{r0}+\sum_{j=1}^{\infty}\Lambda_{rj}\cos\left[jN_r\left(\theta_s-\theta_r\right)\right] \tag{6}$$

where θ_r is the mechanical position of rotor axis relative to the phase A winding axis. N_r is the rotor pole number, and the equivalent air-gap length $\delta(\theta_s, \theta_r)$ can be represented by

$$\delta(\theta_s,\theta_r)=a_0+\left\{\sum_{n=1}^{\infty}a_n\cos\left[nN_s\left(\theta_s-\theta_r\right)\right]+b_n\sin\left[nN_s\left(\theta_s-\theta_r\right)\right]\right\} \tag{7}$$

where the coefficients a_0, a_n and b_n are expressed as

$$a_0=\frac{R_{ro}(\pi\beta_r)^2}{6N_r} \tag{8}$$

$$a_n = -\frac{R_{ro}}{2N_r n^2}\left[\left(1+\cos\left(2\pi\beta_r\right)\right)-\frac{1}{\pi n\beta_r}\sin(2\pi n\beta_r)\right] \quad (9)$$

$$b_n = \frac{R_{ro}}{2N_r n^2}\left[\frac{1}{\pi n\beta_r}\left(1-\cos\left(2\pi\beta_r\right)\right)-\sin(2\pi n\beta_r)\right] \quad (10)$$

where β_r denotes the rotor slot opening ratio, R_{ro} is the rotor outer radius.

Similarly, the air-gap permeance considering the stator slotting can be formatted as [30]

$$\Lambda_s\left(\theta_s\right) = \frac{\mu_0}{g+\delta(\theta_s)} \quad (11)$$

Finally, the resultant airgap permeance function due to the stator and rotor slotting can be written as

$$\Lambda\left(\theta_s,\theta_r\right) = \frac{g\Lambda_s\left(\theta_s\right)\Lambda_r\left(\theta_s,\theta_r\right)}{\mu_0} \quad (12)$$

(2) Biased Flux Modulation Effect

The air-gap flux density $B_{g2}(\theta_s, \theta_r)$ of the CP-FRM can be obtained by introducing a slotted air-gap relative permeance, which can be expressed by multiplying B_{m2} in (3) and the relative air-gap permeance $\Lambda_{rel}(\theta_s, \theta_r)$ [30] [31]

$$B_{g2}\left(\theta_s,\ \theta_r\right)=B_{m2}\Lambda_{rel}\left(\theta_s,\theta_r\right) \quad (13)$$

with

$$\Lambda_{rel}\left(\theta_s,\theta_r\right)=\frac{\Lambda\left(\theta_s,\theta_r\right)}{\left[\mu_0 / \left(1+\dfrac{h_m}{\mu_r}\right)\right]} \quad (14)$$

By substituting (3)~(12) into (13) and (14), it yields

$$B_{g2}\left(\theta_s,\ \theta_r\right)=\sum_{i=1}^{\infty}\sum_{j=1}^{\infty}B_{ij}\left\{\begin{array}{l}\cos\left[(iN_s+jN_r)\theta_s-jN_r\theta_r\right]\\ -\cos\left[(iN_s-jN_r)\theta_s+jN_r\theta_r\right]\end{array}\right\} \quad (15)$$

where B_{ij} can be represented as

$$B_{ij} = \frac{1}{2}B_{m2}\Lambda_{relj} \quad (16)$$

The phase-EMF can be obtained by using the winding function [13]

$$E_{ph}\left(\theta\right) = -\frac{d}{dt}\left(R_g L_a \int_0^{2\pi/N_s} B_{g2}\left(\theta_s,\theta_r\right)N\left(\theta_s\right)d\theta_s\right) \quad (17)$$

where R_g and L_a are the air-gap radius and the effective stack length, and $N(\theta_s)$ is the winding function, which can be given by

$$N\left(\theta_s\right) = \sum_{n=1,3,5,\ldots}^{\infty}\frac{2}{n\pi}\frac{N_a}{P_a}k_{wn}\cos\left(nP_a\theta_s\right) \quad (18)$$

where N_a is the winding turns per phase, P_a is the pole pair number of the armature winding, and k_{wn} is the winding factor of n^{th} harmonic. It should be noted that all stationary PM MMF harmonics and only rotating fundamental permeance, i.e., j=1, can contribute to the back-EMF and torque production [13] [14], whereas, the others will induce the pulsating torque. Furthermore, in order to contribute to the back-EMF, and generate steady electromagnetic torque, the pole pair number of the armature winding P_a should satisfy [17] [29]

$$P_a=iN_s \pm N_r, i=1,2,3,\ldots \quad (19)$$

It should be noted that since only those PM field harmonics with odd orders (i=1, 3, 5,..) exist in in the SPM case, less effective armature field harmonics are responsible for the torque generation.

As the saliency ratio of the stator excited reluctance torque is unity, the average electromagnetic torque T_e can be obtained as

$$T_e = \sum_{i=A,B,C}E_{phi}\left(\theta\right)I_i\left(\theta\right) \quad (20)$$

where $I_i(\theta)$ is the three-phase armature current. As a result, by substituting (13)~(19) into (20), the torque expression can be rewritten as

$$T_e = \frac{\frac{3}{2}R_g L_a N_a N_r I_s}{\left[\mu_0 / \left(1+\dfrac{h_m}{\mu_r}\right)\right]}\sum_{i=1}^{\infty}B_{m2i}\Lambda_{r1}\left(\frac{k_{wa}}{|a|}+\frac{k_{wb}}{|b|}\right) \quad (21)$$

with

$$a=iN_s+N_r \quad (22)$$

$$b=iN_s-N_r \quad (23)$$

where B_{m2i} is the Fourier coefficient of the ideal air-gap flux density B_{m2}, I_s is the RMS value of phase current. Therefore, for the CP-FRM, the air-gap field harmonics having those orders of "$iN_s \pm N_r$, i=1, 2, 3…" engage in the effective torque production. Moreover, it can be generalized that the torque capability is predominantly determined by the rotor pole number, the PM MMF harmonic order and the corresponding winding factor, as long as the basic design parameters are pre-determined.

The analytical and FE predicted open-circuit radial air-gap flux density waveforms and the corresponding harmonic spectra are plotted in Fig. 17. Basically, the analytical results agree satisfactorily with the FE predictions, despite the slight discrepancy due to the fact that the localized magnetic saturation and flux leakage are neglected in the analytical method. It can be observed that the CP machine exhibits higher low-order harmonics, e.g. 1st, 5th and 17th, as well as comparable 7th harmonic than its SPM counterparts, which are the main contributor for the effective torque production, as evidenced in (19). Overall, more abundant harmonics, such as 1st and 23rd for "i=2" in (22) and (23), can be produced in the CP-FRM rather than the SPM structure, which is responsible for its torque improvement. This so-called biased flux modulation phenomenon is mainly attributed to the asymmetric PM flux density distribution of the CP structure, as indicated in Fig. 18.

(3) Torque Production Mechanism

The torque contribution due to individual harmonic can be analytically calculated based on (21)~(23). For instance, in the case of "i=1", it indicates that the modulated air-gap fields derived from the fundamental PM harmonic are considered, and the pole pair numbers of the resultant rotating air-gap harmonics can be obtained based on (22) and (23), i.e., 5 and 17, respectively. Subsequently, the torque contributions due to 5th and 17th air-gap field harmonics can be computed based on (21). The key parameters and the torque components due to each air-gap field harmonic are computed and listed in Table II in order to quantify and provide a powerful insight for the torque contribution. Overall, it demonstrates that the dominant torque contributors concentrate on the 5th harmonic for the two SPM-FRMs, which is produced by the interaction between the fundamental magnet MMF and the fundamental permeance. In addition, it should be noted that although the SPM machines show higher 6th and 18th field harmonics deriving from the fundamental and third harmonics of magnet MMF, these flux harmonics are stationary, and hence not produce back EMF and torque. The torque improvement of the CP-FRM is mainly due to the conspicuous contribution of the 1st harmonic. Based on the abovementioned analyses, the torque performance mechanism of the developed CP-FRM over the SPM counterparts has been successfully analytically unveiled, and confirmed by FE results.

In addition, the open-circuit back-EMFs of the two machines are plotted in Fig. 18, respectively. Obviously, the CP machine exhibits the higher EMF magnitude. Besides, the FE-predicted results agree well with those analytical ones, which confirms the effectiveness of the analytical model.

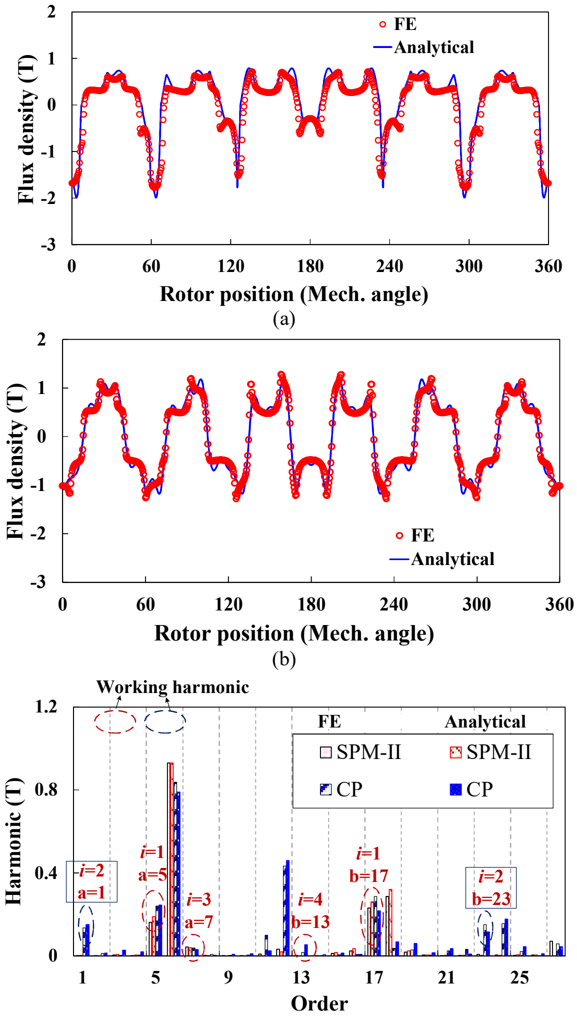

(a)

(b)

(c)

Fig. 17. Comparison of analytical and FE-predicted open-circuit air-gap flux density waveforms. (a) Waveforms, SPM-FRM-II. (b). Waveforms, CP-FRM (c) Harmonic spectra.

TABLE II
COMPARISON OF AIR-GAP FIELD HARMONIC CONTRIBUTIONS TO ELECTROMAGNETIC TORQUE OF 6/11-POLE FRMS WITH SPM AND CP ARRANGEMENTS

Machine types		SPM-I	SPM-II	CP
Source	Pole pair	Magnitude and torque contribution (T/%)		
i=1	a=5	**0.16T (68.35%)**	**0.16T (69.29%)**	**0.24T (21.51%)**
	b=17	**0.23T (28.90%)**	**0.22T (28.02%)**	**0.29T (7.64%)**
i=2	a=1	0.002T2 (1.81%)	0.002T (1.75%)	**0.14T (62.73%)**
	b=23	0.007T (0.02%)	0.008T (0.02%)	0.16T (3.12%)
i=3	a=7	0.04T (0.003%)	0.04T (0.003%)	0.05T (3.20%)
	b=29	0.05T (0.002‰)	0.06T (0.002‰)	0.04T (0.62%)
i=4	a=13	0.003T (1.1E-09%)	0.003T (1.6E-09%)	0.017T (0.62%)
	b=35	0.001T (1.1E-09%)	0.002T (2.8E-09%)	0.002T (0.03%)
Total torque (Nm)		FE/Analytical results		
		1.25/1.21	1.31/1.28	4.92/4.76

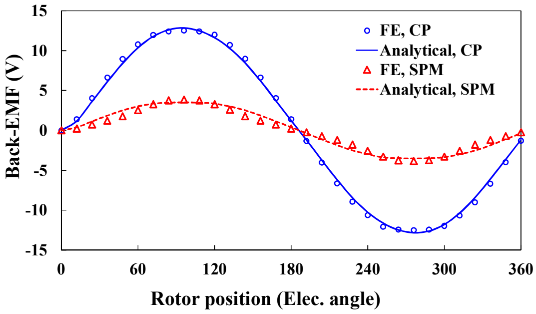

Fig. 18. Open-circuit phase back-EMFs of the SPM- and CP-FRMs (400r/min).

IV. DESIGN PRINCIPLE

A. Winding Configuration

The winding layout of the CP-FRM can be determined by the pole pair number of the armature winding, as expressed in (15). It is worth mentioning that all the field harmonics of the CP-FRM share the same star of slots, and hence identical winding configuration [14]. In particular, by specifying *i*=1 in (22) and (23), it yields

$$P_a = N_s \pm N_r, i = 1, 2, 3, \ldots \tag{24}$$

It suggests that the winding pole pair number P_a of the developed CP-FRM is the same as that of the vernier machine with rotor pole pair number of "N_r" [21]. In other words, the CP-FRM shares identical winding configuration of conventional rotor PM machine, which is quite different from switched flux machines and doubly salient machines. By way of example, the general winding layouts of the 6-stator-slot CP-FRM with different rotor-pole numbers are illustrated in Fig. 19. This winding configuration law can be analogously extended to the other stator-slot/rotor-pole number combinations.

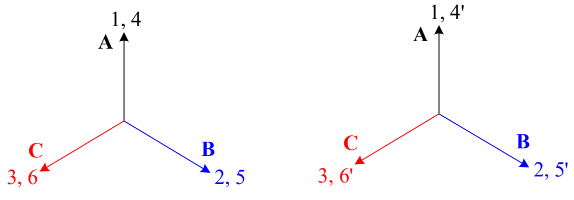

(a) (b)

Fig. 19. Illustration of general winding configurations and EMF coil vectors of 6-stator-slot CP-FRM. (a) N_r=kN_s±2 or 4. (b) N_r=kN_s±1 or 5, k=0, 1, 2…

Similar to conventional PM machines [29], the distribution factor k_d of the stator windings can be given by

$$k_d = \frac{\sin(Qk\alpha/2)}{Q\sin(k\alpha/2)} \tag{25}$$

where Q is the number of the least EMF vectors per phase, α is the angle between two adjacent vectors, and k is the order of EMF harmonic. In addition, the coil pitch factor as a function of stator/rotor pole numbers (N_s/N_r) can be expressed as

$$k_p = \cos\left[\frac{k\pi}{2}\left(\frac{2N_r}{N_s}-1\right)\right] \tag{26}$$

B. Optimal Stator-Slot/Rotor-Pole Number Combination

The feasible stator-slot/rotor-pole number combination can be generally expressed as

$$\frac{N_s}{GCD(N_s,N_r)} = kN_{ph},\ k=1,2,3,... \tag{27}$$

where N_{ph} is the phase number. The relationship between the stator-slot/rotor-pole number combinations N_s/N_r for obtaining symmetrical phase back-EMF of the CP-FRM should comply with [17]

$$\frac{N_s}{GCD(N_s,N_r)} = 2k,\ k=0,1,2,... \tag{28}$$

where GCD denotes the greatest common divisor.

Based on (21)~(26), the torque equation can be further rewritten as

$$T_e = \frac{\frac{3}{2}R_g L_a N_a I_s}{\left[\mu_0 / \left(1+\frac{h_m}{\mu_r}\right)\right]} \sum_{i=1}^{\infty} \frac{1}{\left| i\frac{N_s}{N_r} \pm 1\right|} B_{m2i}\Lambda_{r1}\cos\left[\frac{\pi}{2}\left(\frac{2N_r}{N_s}-1\right)\right] \tag{29}$$

It should be noted that if the basic design parameters, such as the overall dimensions and magnet sizing, etc. are pre-determined in this case, the permeance and PM flux density harmonic magnitudes can be subsequently regarded as constant. Consequently, it can be deduced from (30) that the torque capability reaches the maximum when the following expressions are satisfied:

$$i\frac{N_s}{N_r} \pm 1 \approx 0,\ i.e.,\ N_r \approx iN_s,\ i=1,2,3,... \tag{30}$$

$$2\frac{N_r}{N_s} - 1 \approx 2k,\ i.e.,\ N_r \approx \frac{(2k+1)}{2}N_s,\ k=0,1,2,... \tag{31}$$

By synthesizing (30) and (31), the optimal relation between the stator/rotor pole number combination should comply with "$2N_r$≈kN_s, k=1, 2, 3…"

By way of example, the corresponding pole pair number, pitch factor, distribution factor, winding factor k_w and magnitudes regarding of the main field harmonics of the CP-FRM with different rotor pole number combinations are listed in Table III. It is worth mentioning that all working field harmonics are with same winding factors, as mentioned earlier. Moreover, the magnitudes of the dominant air-gap magnetic fields decrease dramatically when the rotor pole number exceeds 16, which is mainly attributed to significant flux leakage in those cases.

TABLE III
COMPARISON OF MAGNITUDES AND WINDING FACTORS OF DOMINANT WORKING FIELD HARMONICS IN 6-STATOR-SLOT CP-FRMS WITH DIFFERENT ROTOR POLES, K=0, 1, 2…

N_s	N_r	Pole pair	k_d	k_p	k_w	B_g'
6	4	*2*	1	0.866	0.866	0.27 T
		8	1	0.866	0.866	0.16 T
	5	*2*	1	0.500	0.500	0.19 T
		7	1	0.500	0.500	0.14 T
	7	*1*	1	0.500	0.500	0.27 T
		7	1	0.500	0.500	0.13 T
	8	*2*	1	0.866	0.866	0.28 T
		8	1	0.866	0.866	0.14 T
	10	*2*	1	0.866	0.866	0.15 T
		4	1	0.866	0.866	0.25 T
	11	*1*	1	0.500	0.500	0.14 T
		5	1	0.500	0.500	0.24 T
	13	*1*	1	0.500	0.500	0.13 T
		7	1	0.500	0.500	0.22 T
	14	*2*	1	0.866	0.866	0.19 T
		8	1	0.866	0.866	0.14 T
	16	*2*	1	0.866	0.866	0.18 T
		4	1	0.866	0.866	0.16 T
	17	*1*	1	0.500	0.500	0.08 T
		5	1	0.500	0.500	0.03 T
	19	*1*	1	0.500	0.500	0.09 T
		5	1	0.500	0.500	0.05 T
	20	*2*	1	0.866	0.866	0.01 T
		4	1	0.866	0.866	0.02 T

By taking 6-stator-slot CP-FRM as a unity machine, the FE and analytical predicted average torques as functions of the rotor pole number are shown in Fig. 20, in which good agreement between FE and analytical results confirms the validity of the analytical method. In addition, the maximum torque can be observed in the 11-rotor case (N_r≈$2N_s$), which verifies the above theoretical analyses. It should be noticed that the design principle can be further extended to the other stator-slot/rotor-pole number combinations of similar stator excited reluctance machines.

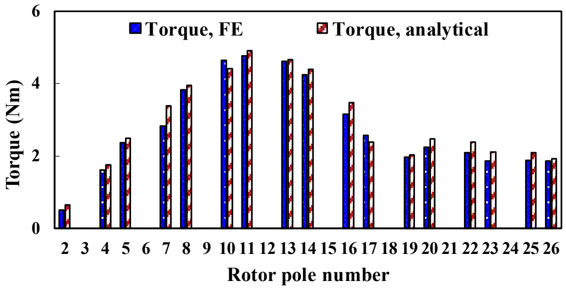

Fig. 20. Variations of FE and analytically predicted average torques with the rotor pole number of the 6-stator-slot CP-FRMs.

C. Effect of Magnet Height

The influence of the magnet thickness h_m on the torque capability of two SPM- and CP-FRMs are evaluated as shown in Fig. 21(a). It demonstrates that the optimal "h_m" of the SPM is smaller. Meanwhile, the torque capability dramatically drops as h_m exceeds the optimal value, while the torque profile tends to decrease steadily for the CP case. Overall, the CP-FRM shows significantly higher torque than its SPM counterpart due to the dominant contribution of the fundamental air-gap field harmonic, as evidenced in Fig. 21(b), which confirms the validity of the abovementioned analytical method.

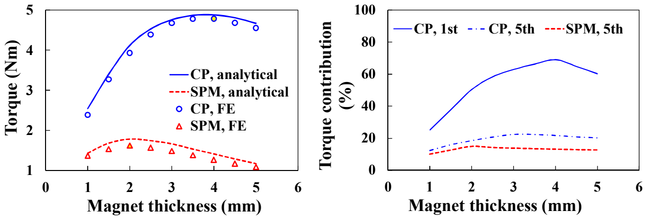

(a) (b)

Fig. 21. Influences of magnet thickness on (a) torque capability, and (b) Torque contributions due to the dominant field harmonics.

V. PERFORMANCE COMPARISON OF CP-FRM, CONVENTIONAL SPM MACHINE AND SWITCHED RELUCTANCE MACHINES

In this paper, the electromagnetic characteristics of a conventional 6 stator slot/4 pole pairs surface-mounted PM (SPM) machine, a 6/4-pole switched reluctance machine (SRM) and the 6/11-pole CP-FRM presented in this paper are compared. The corresponding machine topologies are shown in Fig. 22. In order to perform the comparison fairly, these machines are assumed with identical outer diameter, stack length, air-gap length, and rated current. Meanwhile, the three machines are all optimized for obtaining the largest torque capability with the constraint of rated copper loss of 20W. Furthermore, double-layer non-overlapping windings are employed for these three topologies. The main design specifications of optimally designed machines are listed in Table IV.

The torque performance of the three machines are compared in Figs. 23 and 24. It should be noted that the CP-FRM and SPM machine are both supplied by a standard three-phase full bridge AC inverter, while the SRM is driven by the current chopping control. A circuit composing of a voltage source and a three-phase switching circuit, and it supplies square wave voltage depending on ON/OFF timing to drive the SRM. Form the steady-state torque waveforms in Fig. 23, it can be seen that the CP-FRM exhibits comparable torque capability with the SPM machine at rated load, which is much higher than that of the SRM. Besides, the SRM and SPM machines suffer from more significant torque ripple than the CP-FRM. From the torque and torque/cost ratio against current curves in Fig. 24, the highest over-loading capability can be observed in the SPM case, while the best torque utilization efficiency can be obtained with the CP-FRM design.

The key characteristics and costs of the three machines are listed in Table V. It can be observed that the CP-FRM shows the best torque quality and cost-effectiveness, i.e., its highest torque per magnet volume/cost characteristics. Meanwhile, the regular SPM machine exhibits the lowest iron loss and the highest efficiency. Quantitatively, in terms of cost issues, the SRM can save \$27 for the magnet cost and \$42 compared to the CP-FRM and the regular SPM machine with same volume. Besides, the total cost of the SRM (\$30) is only approximately 52.63% and 41.67% of those of the CP-FRM (\$57) and the regular SPM machine (\$72). Therefore, it can be summarized that the SRM is favorable for low-cost and harsh applications due to the absence of PMs, albeit with low torque density and high torque ripple.

TABLE IV
MAIN DESIGN SPECIFICATIONS OF THE 6 STATOR SLOT/4 POLE PAIRS REGULAR SPM MACHINE AND 6/4-POLE SRM

Parameters	Regular SPM	SRM
Rated speed (r/min)	400	
Outer diameter of stator (mm)	100	
Split ratio	0.60	0.62
Air-gap length (mm)	0.5	
Active stack length (mm)	50	
Stator tooth width (mm)	10	11.5
Ratio of rotor pole to pitch	1	0.45
Rated current (Arms)	7.5	
Turns of winding per phase	132	
NdFeB magnet thickness (mm)	3.6	-
NdFeB magnet grade	N35SH	
Steel material	35CS440	

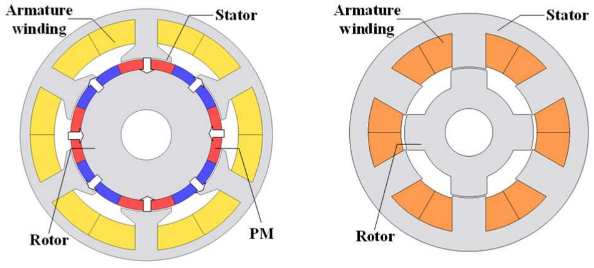

(a) (b)

Fig. 22. Topologies of (a) 6/8-pole regular SPM machine and (b) 6/4-pole SRM.

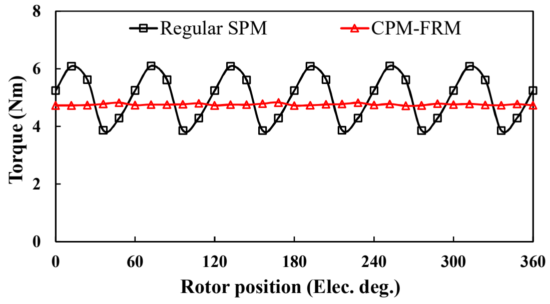

(a)

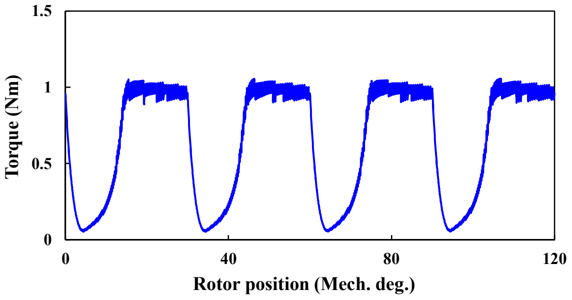

(b)

Fig. 23. Comparison of steady-state torque waveforms under rated-load state, 400r/min. (a) Regular SPM machine and CP-FRM. (b) SRM.

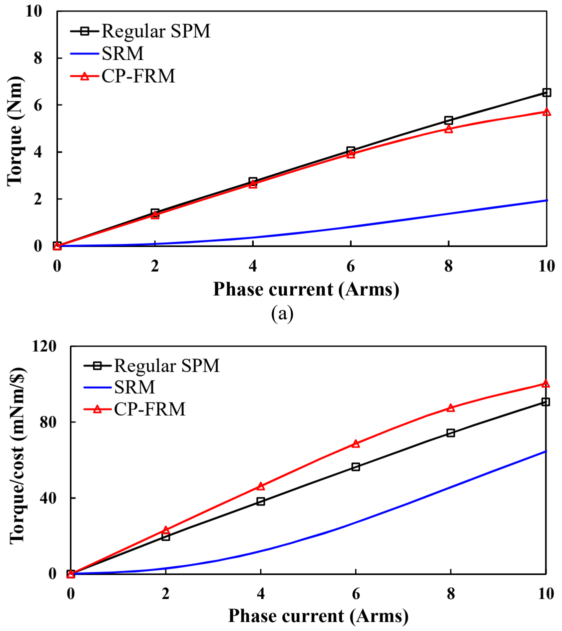

(b)

Fig. 24. Comparison of (a) torque versus current characteristics, and (b) torque/cost ratio against current characteristics.

TABLE V
COMPARISON OF KEY PERFORMANCE METRICS OF THE THREE INVESTIGATED MACHINES @ OPEN-CIRCUIT OR RATED-LOAD STATES

Items	Unit	CP-FRM	Regular SPM	SRM
Average torque	N·m	4.76	5.03	0.65
Torque ripple	%	2.4	44.6	154.4
Cogging torque	mNm	79.9	1137.6	-
Magnet usage	mm^3	24881.4	39230.5	-
Magnet cost	\$	27	42	-
Total cost	\$	57	72	30
Torque/PM volume	N·m/cm^3	0.191	0.128	-
Torque/cost	N·m/\$	0.084	0.070	0.022
Iron loss	W	10.21	6.69	8.72
Efficiency	%	82.65	84.36	70.90

VI. EXPERIMENTAL VALIDATION

The 6-stator-slot/11-rotor-pole CP-FRM is selected for the prototype manufacturing due to its satisfactory torque quality. The machine assembly and test rig are shown in Fig. 25. OSOKKI TS-7700 Torque Station is utilized to generate a load torque for the tested prototypes.

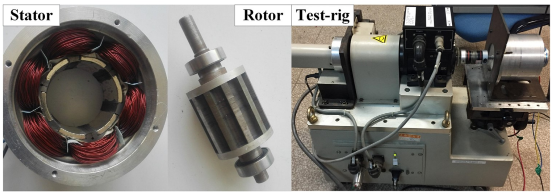

(a) (b)

Fig. 25. (a) 6/11-pole CP-FRM prototype. (b) Test-rig.

Under the rated speed of 400r/min, the phase back-EMFs and torques versus q-axis current characteristics for the prototype machine are measured and compared with FE and analytical results in Fig. 26. The slight difference between FE, analytical and measured results is mainly attributed to the fact that end-effects and mechanical tolerance are not included in the FE and analytical analyses. Under the rated speed of 400r/min, the FE-predicted and measured phase current and voltage waveforms of the prototype machine at rated load condition are shown in Fig. 27. It can be seen that the FE-predicted results agree well with the measured ones. Meanwhile, the on-load current/voltage waveforms are basically sinusoidal, and the phase voltage amplitude is about 24V while the current amplitude is 10A. In addition, the FE-predicted and measured phase inductances versus rotor position curves are shown in Fig. 28. The FE predicted inductances agree well with the test results, although with a discrepancy caused by end windings and manufacturing imperfection. The FE-predicted and measured instantaneous torque waveforms under different q-axis currents are shown in Fig. 29. The corresponding average torques and torque ripple rates obtained by FE method and test are listed in Table VI. The measured torque profiles show good agreement with the FE-predicted ones albeit with slight discrepancy due to the measurement error, friction and minor disturbance in the current waveform. Meanwhile, the measured torque ripples are slightly larger than those predicted by FE, which are mainly attributed to the friction and vibration disturbance caused by the test rig. Overall, it demonstrates that the CP-FRM prototype can provide smooth torque production. Overall, good agreement between analytical, FE and test results confirms the foregoing theoretical analyses.

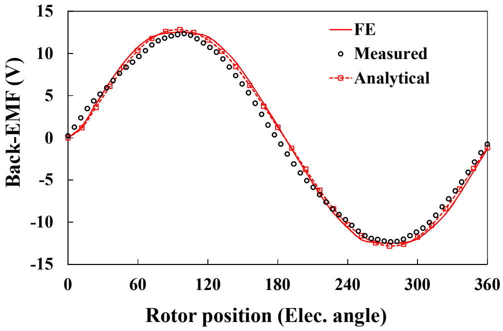

(a)

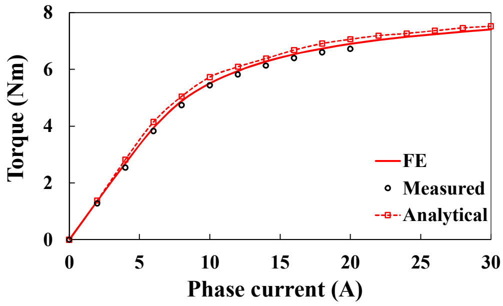

(b)

Fig. 26. Comparison of FE-/analytical-predicted and measured results of the CP-FRM. (a) Back-EMF@400r/min. (b) Torque against current waveform.

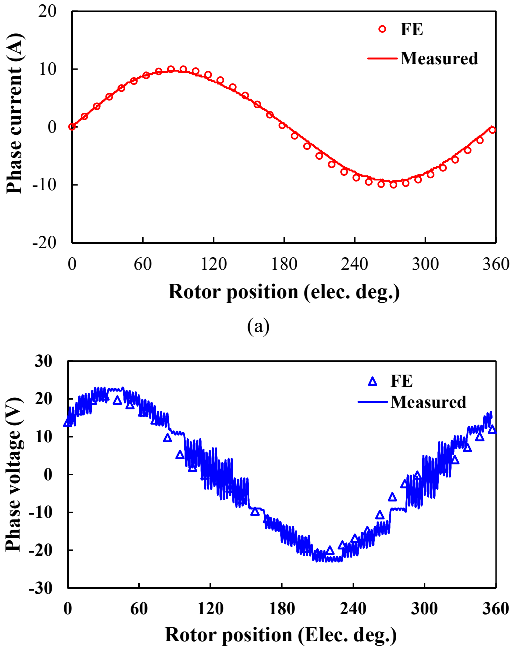

(a)

(b)

Fig. 27. Comparison of FE-predicted and measured phase current and voltage waveforms at rated-load, 400r/min. (a) Phase current. (b) Phase voltage.

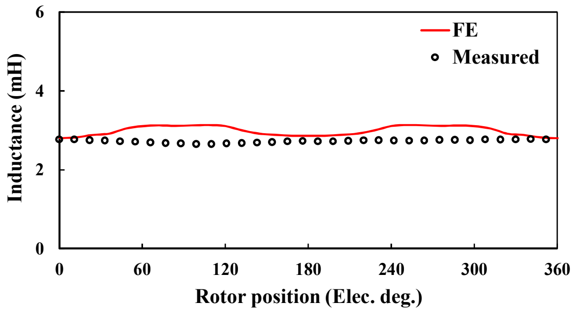

Fig. 28. Comparison of FE-predicted and measured phase inductance versus rotor position waveforms.

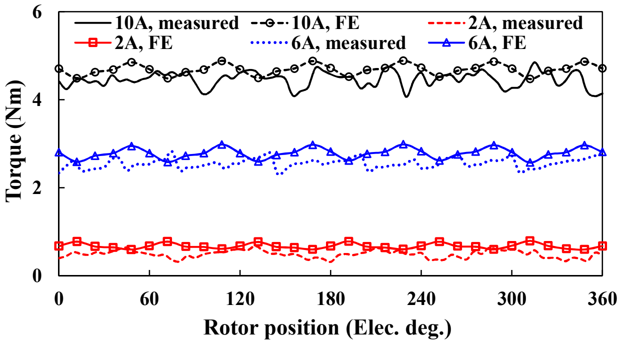

Fig. 29. Comparison of FE-predicted and measured instantaneous torque waveforms under different q-axis currents.

TABLE VI

COMPARISON OF FE-PREDICTED AND MEASURED TORQUE CHARACTERISTICS UNDER DIFFERENT *Q*-AXIS CURRENTS

Q-axis current (A)	Average torque (N·m)		Torque ripple rate (%)	
	FE	Measured	FE	Measured
2	0.63	0.48	8.55	11.20
6	2.73	2.57	3.25	4.25
10	4.62	4.45	2.40	6.13

VII. CONCLUSIONS AND DISCUSSIONS

In this paper, a consequent-pole flux reversal machine (CP-FRM) is analyzed with biased flux modulation theory, and its general working mechanism and design principle are comprehensively investigated. The key findings are summarized as follows:

1) The optimal θ_{mw} for maximizing the torque capability is 30 mechanical degrees for both SPM- and CP-FRMs. The CP-FRM-III can deliver the highest average torque with the lowest torque ripple by using even 28% lower magnet usage than the SPM-FRM-II. Meanwhile, the SPM-FRM-II shows slightly higher torque capability than the SPM-FRM-I. The highest torque ripple can be observed in the CP-FRM-I and CP-FRM-II cases.

2) The torque production mechanism of the CP-FRM lies on the biased flux modulation effect, i.e., its asymmetric air-gap field distribution produces more abundant harmonics responsible for torque generation, which is proved to be the main contributor for torque improvement over its SPM counterpart.

3) The air-gap field harmonics having those orders of $iN_s \pm N_r$ (i=1, 2, 3…) engage in the effective torque production. Moreover, all field harmonics share identical winding configurations, which are same as those of conventional rotor-PM machine with N_r rotor pole pair.

4) The torque capability of the CP-FRM is mainly determined by the ratio of N_s to N_r, the PM MMF harmonic order and the corresponding winding factor. It can be found that their optimal relationship is "$2N_r \approx kN_s$, k=1, 2, 3, 4…", and 11-rotor case ($N_r \approx 2N_s$) is preferred for 6-stator machine.

5) The analytical and FE analyses are validated by the experiments on a 6-stator-slot/11-rotor-pole CP-FRM prototype.

In terms of the application aspects, the CP-FRM can be considered as a particular case of FRM, which is potentially suitable for automotive generator [8], rooftop wind power generation [9] [10], low-speed servo drives [11], direct-drive [12] and electric vehicle applications [20], etc. Specifically, it is reported that FRM can achieve a good performance as an automotive generator due to its robust and simple rotor, as well as ease of manufacturing [8]-[11]. Besides, FRM exhibits fast transient response and immunity of the transient speed change due to low self-inductance [8]. In addition, an outer-rotor FRM is presented for low-power rooftop wind power generation due to its high fault tolerance capability and robust rotor structure, which are suitable for the extreme rooftop environment [9]. The FRM for low-speed servo drive application is introduced by Prof. I. Boldea, et al in 2002 [11], it is found that the FRM can achieve high torque density with less than 3% torque pulsation. Moreover, FRM is recognized as a competitive candidate for electric vehicular applications due to its wide speed range and large torque density [20]. It is worth mentioning that since the CP-FRM presented in this paper can deliver higher torque by using less magnet usage compared to the conventional SPM-FRMs, it is also suitable for those applications requiring high cost-effectiveness.

REFERENCES

[1] T. J. E. Miller, Switched reluctance motors and their control. U.K. Oxford University Press, 1993.

[2] I. Boldea, L. N. Tutelea, L. Parsa, and D. Dorrell, "Automotive electric propulsion systems with reduced or no permanent magnets: an overview," *IEEE Trans. Ind. Electron.*, vol. 61, no. 10, pp. 5696-5711, Oct. 2014.

[3] M. Cheng, W. Hua, J. Zhang, and W. Zhao, "Overview of stator permanent magnet brushless machines," *IEEE Trans. Ind. Electron.,* vol. 58, no. 11, pp.5087-5101, Nov. 2011.

[4] Z. Zhang, Y. Tao, and Y. Yan, "Investigation of a new topology of hybrid excitation doubly salient brushless DC generator," *IEEE Trans. Ind. Electron.*, vol. 59, no. 6, pp. 2550–2556, Jun. 2012.

[5] P. Andrada, B. Blanque, E. Martinez, and M. Torrent, "A novel type of hybrid reluctance motor drive," *IEEE Trans. Ind. Electron.*, vol. 61, no. 8, pp. 4337-4345, Aug. 2014.

[6] Y. Liao, F. Liang, and T. A. Lipo, "A novel permanent magnet motor with doubly salient structure," *IEEE Trans. Ind. Appl.*, vol. 31, no. 5, pp. 1069-1078, Sep./Oct. 1995.

[7] R. P. Deodhar, S. Andersson, I. Boldea, and T. J. E. Miller, "The flux-reversal machine: a new brushless doubly-salient permanent magnet machine," *IEEE Tans. Ind. Appl.*, vol. 33, no. 4, pp. 925-934, Jun. /Aug. 1997.

[8] C. X. Wang, I. Boldea, and S. A. Nasar, "Characterization of three phase flux reversal machine as an automotive generator," *IEEE Trans. Energy Convers.*, vol. 16, no. 1, pp. 74-80, Mar. 2001.

[9] D. S. More, H. Kalluru, and B. G. Fernandes, "Outer rotor flux reversal machine for rooftop wind generator," in *Conf. Rec. IEEE IAS Annu. Meeting*, Edmonton, AB, Canada, pp. 1-6.

[10] C. H. T. Lee, K. T. Chau, and C. Liu, "Design and analysis of a cost-effective magnetless multiphase flux-reversal DC-field machine for wind power generation," *IEEE Trans. Energy Convers.*, vol. 30, no. 4, pp. 1565-1573, Dec. 2015.

[11] I. Boldea, J. Zhang, and S. A. Nasar, "Theoretical characterization of flux reversal machine in low-speed servo drives-the pole-PM configuration," *IEEE Tans. Ind. Appl.*, vol. 38, no. 6, pp. 1549-1557, Nov. /Dec. 2002.

[12] C. H. T. Lee, K. T. Chau, C. Liu, T. W. Ching, and M. Chen, "A new magnetless flux-reversal HTS machine for direct-drive application," *IEEE Trans. Appl. Supercond.* vol. 25, no. 5, Art. No. 5203105, Jun. 2015.

[13] D. S. More, and B. G. Fernandes, "Analysis of flux-reversal machine based on fictitious electrical gear," *IEEE Trans. Energy Convers.*, vol. 25, no. 4, pp. 940-947, Dec. 2010.

[14] H. Y. Li, Y. Liu, and Z. Q. Zhu, "Comparative study of air-gap field modulation in flux reversal and vernier permanent magnet machines," *IEEE Tran. Magn.*, in press.

[15] T. H. Kim, S. H. Won, K. Bong, and J. Lee, "Reduction of cogging torque in flux-reversal machine by rotor teeth pairing," *IEEE Trans. Magn.*, vol. 41, no. 10, pp. 3964–3966, Oct. 2005.

[16] Y. Gao, R. Qu, D. Li, and J. Li, "Torque performance analysis of three-phase flux reversal machines," *IEEE Trans. Ind. Appl.*, vol. 53, no. 3, pp. 2110-2119, May. /Jun. 2017.

[17] X. Zhu, W. Hua, W. Wang, and W, Huang, "Analysis of back-EMF in flux-reversal permanent magnet machines by air-gap field modulation theory," *IEEE Trans. Ind. Electron.,* in press.

[18] S. U. Chung, S. H. Moon, D. J. Kim, and J. M. Kim, "Development of a 20-pole–24-slot SPMSM with consequent pole rotor for in-wheel direct drive," *IEEE Trans. Ind. Electron.*, vol. 63, no. 1, pp. 302-309, Jan. 2016.

[19] J. Li, K. Wang, F. Li, S. Zhu, and C. Liu, "Elimination of even-order harmonics and unipolar leakage flux in consequent-pole PM machines by employing N-S-iron-S-N-iron rotor," *IEEE Trans. Ind. Electron.*, in press.

[20] Y. Gao, R. Qu, D. Li, and G. Zhou, "Consequent-pole flux-reversal permanent-magnet machine for electric vehicle propulsion," *IEEE Trans. Appl. Supercond.*, vol. 26, no. 4, 5200105, Jun. 2016.

[21] Y. H. Li, and Z. Q. Zhu, "Analysis of flux-reversal permanent-magnet machines with different consequent-pole PM topologies," *IEEE Trans. Magn.*, in press.

[22] W. Zhao, J. Zheng, J. Wang, G. Liu, J. Zhao, and Z. Yang, "Design and analysis of a linear permanent-magnet vernier machine with improved force density," *IEEE Trans. Ind. Electron.*, vol. 63, no. 4, pp. 2072-2082, Apr. 2016.

[23] H. Yang, H. Lin, Z. Q. Zhu, S. Fang, and Y. Huang, "A novel stator-consequent-pole memory machine," in *Proc. Energy Convers. Congress and Expo. (ECCE)*, 2016 IEEE, Milwaukee, USA, 2016. 9.18-9.22.

[24] H. Yang, S. Lyu, H. Lin, and Z. Q. Zhu, "A variable-mode stator consequent pole memory machine," *AIP Advances*, vol. 8, no. 5, Art. No. 056612, 2018.

[25] H. Yang, H. Lin, Z. Q. Zhu, H. Wang, S. Fang, and Y. Huang, "A novel flux-reversal hybrid magnet memory machine," in Proc. *2017 IEEE Energy Conversion Congress and Exposition (ECCE)*, 2017, pp. 5853-5860. 2017 IEEE, Cincinnati, USA, 2017. 10.1-10.5.

[26] J. Dong, Y. Huang, L. Jin, H. Lin, and H. Yang, "Thermal optimization of a high-speed permanent magnet motor," *IEEE Trans. Magn.*, vol. 50, no. 2, Article. 7018504, Feb. 2014.

[27] M. Cheng, X. Wang, Loss Calculation and thermal analysis for nine-phase flux switching permanent magnet machine," *IEEE Trans. Energy Convers.,* vol. 33, no. 4, pp. 2133-2142, May. 2018.

[28] M. Cheng, P. Han, and W. Hua, "General airgap field modulation theory for electrical machines," *IEEE Trans. Ind. Electron.,* vol. 64, no. 8, pp. 6063-6074, Aug. 2017.

[29] Z. Q. Zhu and Y. Liu, "Analysis of air-gap field modulation and magnetic gearing effect in fractional-slot concentrated-winding permanent-magnet synchronous machines," *IEEE Trans. Ind. Electron.,* vol. 65, no. 5, pp. 3688-3698, May. 2018.

[30] B. Gaussens, O. Barriere, E. Hoang, J. Saint-Michel, P. Manfe, M. Lecrivain, and M. Gabsi, "Magnetic field solution in doubly slotted airgap of conventional and alternate field-excited switched-flux topologies," *IEEE Trans. Magn.*, vol. 49, no. 9, pp. 5083-5096, Sep. 2013.

[31] D. Zarko, D. Ban, and T. A. Lipo, "Analytical calculation of magnetic field distribution in the slotted air gap of a surface permanent-magnet motor using complex relative airgap permeance," *IEEE Trans. Magn.*, vol. 42, no. 7, pp. 1828-1837, Jul. 2006.